

This item is the archived peer-reviewed author-version of:

Efficient Ab initio modeling of dielectric screening in 2D van der Waals materials : including phonons, substrates, and doping

Reference:

Gjerding M.N., Cavalcante L.S.R., Chaves Andrey, Thygesen K.S.- Efficient Ab initio modeling of dielectric screening in 2D van der Waals materials : including phonons, substrates, and doping
The journal of physical chemistry: C : nanomaterials and interfaces - ISSN 1932-7447 - 124:21(2020), p. 11609-11616
Full text (Publisher's DOI): <https://doi.org/10.1021/ACS.JPCC.0C01635>
To cite this reference: <https://hdl.handle.net/10067/1761870151162165141>

Efficient Ab-Initio Based Modeling of Dielectric Screening in 2D Van Der Waals Materials: Including Phonons, Substrates, and Doping

M. N. Gjerding,^{*,†} L. S. R. Cavalcante,[¶] Andrey Chaves,[¶] and K. S. Thygesen[†]

[†]*CAMD, Department of Physics, Technical University of Denmark, 2800 Kgs. Lyngby,
Denmark*

[‡]*Center for Nanostructured Graphene (CNG), Technical University of Denmark, Årstedss
Plads, Bldg. 345C, DK-2800 Kongens Lyngby, Denmark.*

[¶]*Departamento de Física, Universidade Federal do Ceará, Caixa Postal 6030, Campus do
Pici, 60455-900 Fortaleza, Ceará, Brazil*

E-mail: mogje@fysik.dtu.dk

Abstract

The quantum electrostatic heterostructure (QEH) model allows for efficient computation of the dielectric screening properties of layered van der Waals bonded heterostructures in terms of the dielectric functions of the individual two-dimensional (2D) layers. Here, we extend the QEH model by including: (1) Contributions to the dielectric function from infrared active phonons in the 2D layers, (2) screening from homogeneous bulk substrates, and (3) intraband screening from free carriers in doped 2D semiconductor layers. We demonstrate the potential of the extended QEH model by calculating the dispersion of coupled phonons in multilayer stacks of hexagonal boron-nitride (hBN), the strong hybridization of plasmons and optical phonons in graphene/hBN heterostructures, the effect of substrate screening on the exciton series of monolayer MoS₂, and the properties of hyperbolic plasmons in a doped phosphorene sheet. The new QEH code is distributed as a Python package with a simple command line interface and a comprehensive library of dielectric building blocks for the most common 2D materials, providing an efficient open platform for dielectric modeling of realistic vdW heterostructures.

Introduction

Artificially created van der Waals (vdW) heterostructures composed of stacked two-dimensional (2D) crystals have opened new opportunities for designing layered materials with chemical composition and electronic properties sharply defined on a sub-nanometer length scale. A number of novel materials, devices, and physical phenomena based on this concept have already been demonstrated, including light emitting diodes in band structure engineered hBN/graphene/MoS₂ structures,¹ ultrafast photo detectors made of few-layer WSe₂ stacks,² atomically thin solar cells based on MoS₂/WSe₂ heterobilayers,³ vertical tunneling transistors,^{4,5} van der Waals quantum wells composed of multilayer MoS₂ structures,⁶ Mott insulating- and unconventional superconducting states in twisted bilayer graphene,^{7,8} and

much more. In addition, encapsulation in atomically flat hBN has become a standard method to improve the electronic quality of active 2D layers.⁹ Consequently, a proper account of the ubiquitous interlayer (or substrate-) interactions has become an essential ingredient in the theoretical modeling of 2D materials for almost any application.

In determining a material's response to electromagnetic fields, as well as for calculating elementary excitations such as plasmons, phonons, excitons, and quasiparticles, the dielectric function, $\epsilon(\mathbf{r}, \mathbf{r}', \omega)$, plays a fundamental role.¹⁰ Furthermore, it is a well established fact that dielectric properties of 2D materials are extremely sensitive to their environment, e.g. embedding layers or substrates.^{11–13} This is due to the long range nature of the Coulomb interaction and the weak intrinsic screening of the 2D material itself.^{14,15} These circumstances make the determination of the dielectric function of embedded or supported 2D materials a critical prerequisite for a realistic description of their electronic and optical properties. However, conventional first-principles schemes are challenged by the incommensurable nature of most 2D/2D or 2D/substrate interfaces. Due to the weakness of the dispersive layer-layer bonds, the crystal structure at such heterointerfaces can be highly complex, with either no or very large periodicity due to in-plane lattice mismatch or rotational misalignment. For all but the simplest heterostructures, this implies the use of supercells with many hundreds or thousands of atoms,^{7,8,16,17} which makes the problem intractable for standard first-principles methods.

The previously introduced quantum electrostatic heterostructure (QEH) model¹⁸ overcomes the problem of large interface supercells and enables an efficient calculation of the dielectric function of general vdW structures containing hundreds of layers. The fundamental assumption behind the QEH scheme is the additivity of the independent polarizabilities of the individual layers. This approximation, which has proved surprisingly accurate, is trivially fulfilled in the case of zero hybridization between the wave functions on neighboring layers. Recent work¹⁹ has shown that even in the presence of interlayer hybridization the requirement of additivity can still be valid, thus lending extra credibility to the results of

the QEH model even for systems where hybridization is known to be significant.

In a nutshell, the QEH model takes as input a low-dimensional representation of the density response function, $\chi(\mathbf{r}, \mathbf{r}', \omega)$, for each isolated 2D layer of the heterostructure. These quantities are calculated from first principles and are referred to as *dielectric building blocks* (DBB). The dielectric function of the entire vdW heterostructure is subsequently calculated by solving a Dyson-like equation which couples the DBBs via the Coulomb interaction. Computational times are typically on the order of seconds or minutes and scales linearly with the number of momentum and frequency-points at which the response function of the heterostructure should be evaluated.

In the original QEH model, the DBBs were calculated from first principles density functional theory (DFT) including screening from electronic transitions at the level of the random phase approximation (RPA). In this work, we extend the model in three important ways. First, we include the contribution of optical phonons to the dielectric screening. The screening response from phonons governs the dielectric response of polar crystals in the infrared frequency regime. This new feature thus extends the applicability of the QEH model to a new type of materials and frequency regimes. Our implementation uses an analytical model for the lattice dielectric function that depends on the optical phonon frequencies and the Born charges of the atoms both of which are obtained from first principles DFT. Secondly, we add the possibility of accounting for screening from a bulk substrate. This is a rather straightforward but highly useful feature, as most experiments on 2D materials are performed on substrates, such as quartz, fused silica, or SiO_2 . The implementation uses the method of image charges and takes the (local) frequency dependent bulk dielectric constant of the substrate as input. The latter can either be taken from experiments or calculated ab-initio in the case of crystalline substrates. Finally, while the original QEH model only included electronic screening due to interband transitions (for semiconducting layers), the new model can account for intraband screening due to free carriers in the valence or conduction bands. This is important, since 2D semiconductors under most experimental conditions are doped

(intentionally or unintentionally). The method is implemented using a temperature dependent RPA model for the dielectric function of the free carriers in 2D with effective masses obtained from DFT.

In this paper we outline the theory, document the implementation of the new QEH model and illustrate its potential by a number of examples of relevance to recent experiments. For details on the implementation we refer the reader to the supplementary material.

Theory

Basics of the QEH Model

We begin by summarizing the main idea behind the QEH model. More details can be found in Ref.¹⁸ and the associated supplementary material. In general, the (inverse) dielectric function is related to the interacting density response function, χ , via

$$\epsilon^{-1}(\mathbf{r}, \mathbf{r}', \omega) = \delta(\mathbf{r} - \mathbf{r}') + \int \frac{1}{|\mathbf{r} - \bar{\mathbf{r}}|} \chi(\bar{\mathbf{r}}, \mathbf{r}', \omega) d\bar{\mathbf{r}}. \quad (1)$$

The QEH model calculates the density- and dielectric response functions of the heterostructure in two steps. First, the in-plane averaged density response function of each isolated 2D layer of the heterostructure, $\chi_i(z, z', \mathbf{q}_{\parallel}, \omega)$ (i is the layer index), is calculated. For the electronic response we use the random phase approximation (RPA) with DFT-PBE orbitals and energies, but this is not essential and other schemes could be employed. From χ_i we can obtain the density induced by an external potential of the general form

$$\phi(z, \mathbf{q}_{\parallel}, \omega) = f(z) \exp(i\mathbf{r}_{\parallel} \cdot \mathbf{q}_{\parallel}) \exp(i\omega t), \quad (2)$$

In the QEH model we specialize to potentials of the form $f_{\alpha}(z) = (z - z_i)^{\alpha}$ where z_i is the center of layer i and $\alpha = 0, 1$. The two values of α correspond to potentials that are either constant or vary linearly across the layer and we refer to them as monopole and dipole terms,

respectively.

The potentials in Eq. (2) induce monopole ($\alpha = 0$) or dipole ($\alpha = 1$) charge densities in the layer. We have found that the z -profile of the induced densities do not vary much with ω while the magnitude can vary significantly. To separate the two effects we define the z -profile as

$$\rho_{i\alpha}(z, \mathbf{q}_{\parallel}) = C_0 \int \chi_i(z, \bar{z}, \mathbf{q}_{\parallel}, \omega = 0) f_{\alpha}(\bar{z}) d\bar{z} \quad (3)$$

where C_0 is a normalization factor (see below), and the response functions

$$\chi_{i\alpha}(\mathbf{q}_{\parallel}, \omega) = \int f_{\alpha}(z) \chi_i(z, \bar{z}, \mathbf{q}_{\parallel}, \omega) f_{\alpha}(\bar{z}) dz d\bar{z}. \quad (4)$$

The normalization factor C_0 is then determined by requiring

$$\chi_{i\alpha}(\mathbf{q}_{\parallel}, \omega = 0) \rho_{i\alpha}(z, \mathbf{q}_{\parallel}) = \int \chi_i(z, \bar{z}, \mathbf{q}_{\parallel}, \omega = 0) f_{\alpha}(\bar{z}) d\bar{z}. \quad (5)$$

The data set $\{\chi_{i\alpha}(\mathbf{q}_{\parallel}, \omega), \rho_{i\alpha}(z, \mathbf{q}_{\parallel})\}$ for $\alpha = 0, 1$ constitutes the dielectric building block (DBB) of layer i . For isotropic 2D materials, \mathbf{q}_{\parallel} is sampled on a 1D grid. For anisotropic materials, the \mathbf{q}_{\parallel} -dependence is represented by sampling on two 1D grids along two orthogonal directions in reciprocal space. It should be clear that the DBB allows us to compute the induced density due to a general external potential of the form (2) by performing a first order Taylor expansion of f around the center of the layer.

In the second step, the density response function of the vdWH is obtained by solving a Dyson equation that couples the DBBs together via the Coulomb interaction. The Dyson equation for the density response function of the heterostructure reads (omitting the \mathbf{q}_{\parallel} and ω variables for simplicity):

$$\chi_{i\alpha,j\beta} = \chi_{i\alpha} \delta_{i\alpha,j\beta} + \chi_{i\alpha} \sum_{k \neq i, \gamma} V_{i\alpha,k\gamma} \chi_{k\gamma,j\beta} \quad (6)$$

where the Coulomb matrices are defined as

$$V_{i\alpha,k\gamma}(\mathbf{q}_{\parallel}) = \int \rho_{i\alpha}(z, \mathbf{q}_{\parallel}) \Phi_{k\gamma}(z, \mathbf{q}_{\parallel}) dz \quad (7)$$

and $\Phi_{k\gamma}$ is the potential created by the density profile, $\rho_{k\gamma}$. We obtain $\Phi_{k\gamma}$ by solving a 1D Poisson equation with open boundary conditions. Note that we leave out the self-interaction terms in Eq. (6) since the intralayer Coulomb interaction is already accounted for in $\chi_{i\alpha}$. Finally, the (inverse) dielectric function of Eq. (1) in the monopole/dipole basis becomes

$$\epsilon_{i\alpha,j\beta}^{-1}(\mathbf{q}_{\parallel}, \omega) = \delta_{i\alpha,j\beta} + \sum_{k\gamma} V_{i\alpha,k\gamma}(\mathbf{q}_{\parallel}) \chi_{k\gamma,j\beta}(\mathbf{q}_{\parallel}, \omega). \quad (8)$$

We emphasize that the calculated heterostructure response function is that of an isolated heterostructure (or a heterostructure on a substrate - see later). In particular, we do not apply periodic boundary conditions in the out-of-plane direction when solving the Dyson equation (8). Therefore, there is no need to correct for interactions with periodically repeated images as required in supercell approaches. This is, however, important to consider when calculating the response function, $\chi_{i\alpha}$, of the isolated 2D layers.^{20,21} Since we use periodic supercell calculations to obtain the latter we employ an out-of-plane truncated Coulomb interaction to avoid the interaction with periodic images.¹⁸

The QEH method has been benchmarked against experimental exciton binding energies in the original paper.¹⁸ Furthermore, the method has been used to compute EELS spectra of multilayer MoS2 obtaining good agreement with experiments both for excitons and plasmons.²² This concludes our summary of the original implementation of the QEH model. A description of the various extensions to the QEH model now follows.

Lattice polarizability

In addition to the electronic response (corresponding to frozen nuclei), polar materials also respond to external fields via lattice deformations. The contribution from the lattice polarization can be significant for frequencies below or comparable to the optical phonons of the system and can lead to non-trivial effects when coupled to electronic transitions in the same frequency regime. The QEH model has been extended to include this effect.

The lattice contribution to the DBB is obtained from the Born effective charges and Γ -point phonon modes of the isolated 2D material. The Born charges are defined as derivatives of the macroscopic polarization density, $\mathbf{P}(\mathbf{E}, \{\mathbf{u}^a\})$, with respect to atomic displacements under the condition of vanishing macroscopic electric field, \mathbf{E} , (defined as the total electric field averaged over a unit cell of the material).^{23,24} The latter condition ensures that the electron system remains in the ground state during the atomic displacement and is automatically satisfied in a calculation with periodic boundary conditions on the unit cell. When a cell of in-plane area A_{cell} is used to represent the 2D layer, the expression for the Born charges becomes

$$Z_{i,aj} = \frac{e}{A_{\text{cell}}} \frac{\partial P_i}{\partial u_{aj}} \Big|_{E=0}$$

where a denotes an atom and ij are cartesian coordinates. The 2D polarization density, P_i , is obtained following the Berry phase formalism of the modern theory of polarization^{23,24} using a finite difference evaluation of the derivative. We have implemented the method in the open source electronic structure code GPAW²⁵ and used it to compute the Born charges of all the 2D materials in the Computational 2D Materials Database (C2DB)²⁶ with a finite band gap (around 1000 monolayers). The details of the implementation will be published elsewhere.

The lattice polarizability of a 2D material in the optical limit ($\mathbf{q} = \mathbf{0}$) takes the form (see

appendix for a derivation)

$$\alpha_{ij}^{\text{lat}}(\omega) = \frac{e^2}{A_{\text{cell}}} \sum_{ak,bl} Z_{i,ak} [(\mathbf{C} - \mathbf{M}(\omega^2 - i\gamma\omega))^{-1}]_{ak,bl} Z_{j,bl}. \quad (9)$$

where \mathbf{C} is the force constant matrix in the optical limit, \mathbf{M} is a diagonal matrix containing the atomic masses, and γ is a relaxation rate. We emphasise that the polarizability in Eq. (9) is *local*, i.e. \mathbf{q}_{\parallel} -independent. In general we expect this to be an excellent approximation due to a rather weak \mathbf{q}_{\parallel} -dependence of optical phonons (note that the dispersion of the phonon-*polaritons* in Fig. 1 is driven by the macroscopic polarization field in the absence of which the phonons show no dispersion in the considered wave vector range).

To make contact to the QEH formalism we must consider the polarization (per area) induced by a potential, ϕ , of the form (2). Writing $\mathbf{E} = \nabla\phi$ and using that $\nabla \cdot \mathbf{P}$ equals the induced electron density, we can obtain the total monopole and dipole components of the DBB of layer i ,

$$\chi_{i0}^{\text{tot}}(\mathbf{q}_{\parallel}, \omega) = \chi_{i0}^{\text{el}}(\mathbf{q}_{\parallel}, \omega) - q_{\parallel}^2 \alpha_{\parallel\parallel}^{\text{lat}}(\omega) \quad (10)$$

$$\chi_{i1}^{\text{tot}}(\mathbf{q}_{\parallel}, \omega) = \chi_{i1}^{\text{el}}(\mathbf{q}_{\parallel}, \omega) - \alpha_{zz}^{\text{lat}}(\omega) \quad (11)$$

where $\alpha_{\parallel\parallel}^{\text{lat}}$ denotes the 2×2 in-plane submatrix of α^{lat} . When these DBBs are used in Eqs. (6) and (8) we obtain the dielectric response function of the vdWH including both electron and phonon contributions.

In addition to the Born charges, we have calculated the Γ -point phonon modes (including the force constant matrix \mathbf{C}) for all materials in the C2DB. From these data sets, it is straightforward to obtain the lattice polarizability in Eq. (9). We have compiled the full DBBs for a set of 34 semiconducting transition metal dichalcogenides, graphene, phosphorene, and hexagonal boron-nitride, based on data from the C2DB. These DBBs are also freely available and can be found here in Ref.²⁷ Compared to the lattice part, the electronic DBB is computationally more demanding, as it requires *ab-initio* linear response calculations as

function of q_{\parallel} and ω .

Bulk substrates

The inclusion of substrate screening is implemented by the method of image charges. In the absence of a substrate, we obtain the potential generated by an induced density in layer i by solving the 1D Poisson equation (ω - and \mathbf{q}_{\parallel} -variables omitted)

$$\frac{\partial^2}{\partial z^2} \Phi_{i\alpha}(z) - q_{\parallel}^2 \Phi_{i\alpha}(z) = -4\pi \rho_{i\alpha}(z). \quad (12)$$

with open boundary conditions (as usual, α denotes the monopole/dipole index). In the presence of a substrate, situated a distance d below the layer, we must add the potential from the image charge distribution (see supplementary material). The latter is given by²⁸

$$\rho_{i\alpha}^{\text{image}}(z) = -\frac{\epsilon^{\text{sub}}(\omega) - \epsilon_0}{\epsilon^{\text{sub}}(\omega) + \epsilon_0} \rho_{i\alpha}(-z - 2d), \quad (13)$$

where ϵ^{sub} is the frequency-dependent (but wave vector independent) bulk dielectric constant of the substrate. The potential corresponding to $\rho_{i\alpha}^{\text{image}}$ is obtained by a similar scaling/reflection operation on $\Phi_{i\alpha}$. Finally, the image charge potential is then included in the Coulomb interaction that enters the Dyson equation for the heterostructure Eq. (6).

Doped semi-conductors and graphene

Moving on, the QEH model has been extended to improve its descriptions of doped graphene. It is well known that electronic properties of (doped) graphene are extremely difficult to describe accurately by pure *ab-initio* methods because of its highly dispersive linear bands²⁹ that require exceedingly dense k -point grids. As detailed in Sec. S2, to overcome this problem, we construct a DBB for graphene by complementing the *ab-initio* calculated induced density profiles Eq. (3) (which are not k -point sensitive) by an analytical model of the den-

sity response function. In practice, we construct a hybrid graphene DBB by combining the analytical result for the density response function with the induced density obtained from the *ab-initio* response function, see Eq. (3). The latter is well defined even for relatively coarse k -point grids and can easily be interpolated to an arbitrarily fine q -point grid. The above considerations apply to the monopole component of the DBB. As it turns out, the dipole component is not very sensitive to the employed k -point grid and does not require special treatment. The calculations for the plasmon-phonon coupling in graphene/hBN heterostructures presented in Fig. 2 employed a hybrid graphene DBB.

Finally, the QEH model has been extended to account for doping in 2D semi-conductors. Dielectric building blocks for intrinsic 2D semiconductors can be generated straightforwardly from the *ab-initio* response function. Here we have generalized the applicability of the QEH model to doped semiconductors by including contributions from intraband transitions due to the free carriers in the conduction band (for n-type doping) or valence band (for p-type doping) assuming parabolic bands with some effective mass, see Sec. S3. Effective masses, evaluated from the PBE band structure with spin-orbit interaction, are available in the C2DB²⁶ for around 1000 2D semiconductors.

Results and Discussion

Phonon polaritons in hBN multilayers

As an initial example we consider the hybridization of the longitudinal optical (LO) phonons in a 10-layer film of hBN. It is well known that the dielectric function exhibits poles in the (complex) ω -plane at the excitation energies of the system. To unravel the excitation spectrum we calculate the loss function³⁰

$$S(\mathbf{q}_{\parallel}, \omega) = -\text{Im}(\text{Tr}\epsilon^{-1}(\mathbf{q}_{\parallel}, \omega)) \quad (14)$$

where ϵ^{-1} is the dielectric matrix defined by Eq. (8) and the trace is taken over layer- and monopole/dipole indices. The loss function of the hBN slab is shown in Fig. 1(a). The intensity of the spectral peaks is a measure for how strongly the excitation couples to a local potential of the form (2). Due to the large band gap of hBN, the electronic contribution to the dielectric function reduces to a real constant, ϵ^∞ , over the considered frequency regime, and consequently the dielectric response is governed solely by the lattice vibrations. We focus on the energy range of the optical in-plane phonon modes (the dipole carrying out-of-plane optical modes appear in the spectrum just below 100 meV, see flat yellow line in Fig. 2(b-d)). There are ten in-plane TO modes and ten in-plane LO modes. The TO modes are all degenerate with energy, $\hbar\omega_{\text{TO}}$ and show no dispersion (see discussion below). We note that these modes are not seen in the spectrum because they do not couple to fields of the form (2).

In polar bulk crystals the longitudinal- and transverse optical phonon modes (LO and TO) will be split for $q_{\parallel} \rightarrow 0$ due to the finite macroscopic polarization of the LO mode. However, in a 2D material the LO-TO splitting vanishes for $q_{\parallel} \rightarrow 0$ because the electric field produced by the finite macroscopic polarization vanishes in this limit.³¹ This effect is clearly seen in Figure 1. At finite q_{\parallel} , however, the electric field produced by the polar LO phonons leads to significant coupling between them, resulting in the formation of phonon-polariton subbands. The standing wave profile of the subband modes is sketched in Fig. 1(b).

It should be stressed that the observed hybridization of LO phonon modes is an effect of the macroscopic electric field set up by the polar lattice vibrations. It would therefore *not* be captured by a conventional DFT phonon calculation that doesn't explicitly include the macroscopic electric field, which would yield ten degenerate pairs of LO-TO phonon modes. In the DFT description, the dispersion of the modes would be governed by short-range electrostatic and quantum mechanical hybridization effects, while the long range macroscopic field effects would be missed. On the other hand, short-range electrostatics and the quantum mechanical interlayer hybridization is not accounted for by the QEH model. Fortunately,

this type of short-range interlayer phonon coupling is usually very weak in vdW bonded materials³² and can be safely ignored for the purpose of modeling the dielectric properties.

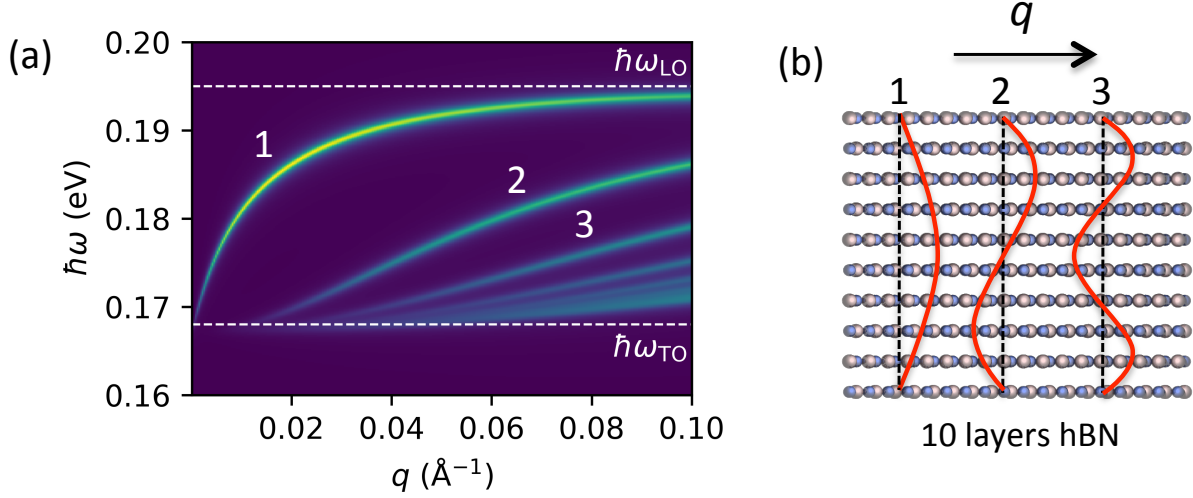


Figure 1: (a) Loss function, cf. Eq. (14), of a 10-layer hBN stack reveals the formation of subbands of longitudinal in-plane phonon-polaritons. The white dashed lines correspond to the in-plane TO and LO frequencies of bulk hBN. The well known breakdown of the LO-TO splitting in the $q \rightarrow 0$ for 2D materials is clearly seen. The strong hybridization of the LO sheet phonons leading to the subband formation is due to the macroscopic polarization field created by the phonons. Numbers label the electric field profile of each subband as sketched in (b).

Phonon-plasmon coupling in graphene/hBN

As another example we consider the coupling of graphene plasmons with the optical phonons in hBN. Experiments have reported that the strong coupling between graphene plasmons and polar phonons can create new hybrid modes with significantly altered dispersion curves.^{33–37} The effect has been reproduced theoretically using semi-classical models.³⁸ In contrast, the approach presented here is fully *ab-initio* subject to the approximations underlying the QEH model; in particular, it is completely parameter free.

In Fig. 2 we show the calculated loss function (14) of four different graphene/hBN heterostructures. For all structures, the graphene sheets are n-doped with a carrier concentration corresponding to $E_F = 0.4$ eV (to obtain an accurate description of the plasmon in

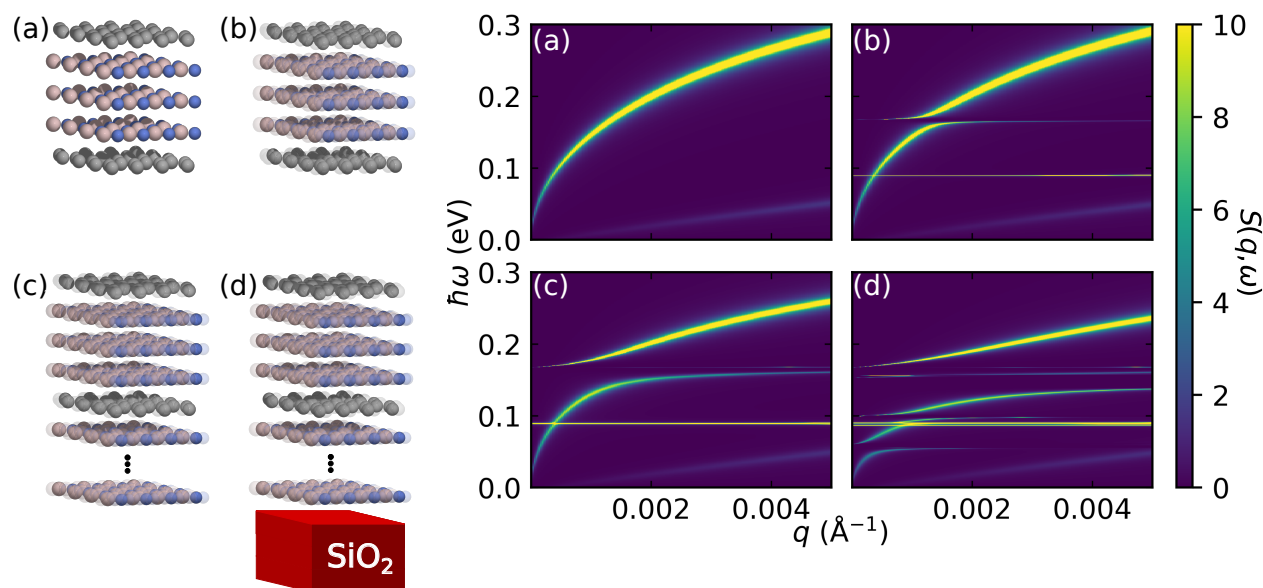


Figure 2: Loss function, cf. Eq. (14), of freestanding and supported graphene/hBN heterostructures. (a) Two doped graphene sheets separated by 3 layers of hBN. Only the electronic response is included in the dielectric building blocks. (b) Same as (a) but with the phonon contribution included in the hBN building blocks as indicated by a blurring of the atoms. (c) Same as (b) but with 18 layers of hBN added below the heterostructure. (d) Same as (c) but with the entire heterostructure placed on a SiO_2 substrate.

the doped graphene layer we employ a hybrid analytical/*ab-initio* DBB as described in Sec. S2). Panel (a) refers to a structure composed by two graphene sheets separated by 3 layers of hBN. For this case phonons are *not* included in the DBB of the hBN layers. The plasmon dispersion presents two branches, corresponding to out-of-plane symmetric and anti-symmetric combinations of the graphene sheet plasmons.

In Fig. 2(b), the phonon contribution is included in the hBN building block. This leads to an anti-crossing where the symmetric plasmon intersects the hBN in-plane LO phonon. The faint line just below 100 meV represents the optical out-of-plane phonons of the hBN sheet. The out-of-plane phonons also couple to the plasmon, but the anti-crossing is very weak and can hardly be seen on this scale, consistent with previous literature showing that the out-of-plane response is generally weak.³⁹ In Fig. 2(c), we added 18 layers of hBN below the heterostructure. This leads to a stronger phonon response, and consequently an enhancement of the anti-crossings with the plasmon. Finally, we place the entire structure

on top of a SiO₂ substrate (see below for details). Despite the fact that the graphene sheets are separated from the substrate by an 18-layer thick hBN film, there is a significant effect on the loss spectrum. In particular, new regions of anti-crossings appear where the plasmon dispersion intersects the three SiO₂ phonon resonances at 55 meV, 98 meV, and 140 meV, respectively.

In the example discussed above, cf. Fig. 2(d), the SiO₂ substrate was included via its dielectric function^{40–42}

$$\epsilon_{\text{SiO}_2}(\omega) = \epsilon_{\infty} + \sum_{j=1}^3 f_j \frac{\omega_{\text{TO},j}^2}{\omega_{\text{TO},j}^2 - \omega^2}, \quad (15)$$

where ϵ_{∞} is the electronic dielectric constant and $\omega_{\text{TO},j}$ is the frequency of the j th transverse optical phonon with $\epsilon_{\infty} = 2.4\epsilon_0$, $f_j = (0.7514, 0.1503, 0.6011)$ and $\omega_{\text{TO},j} = (0.055, 0.098, 0.140)$ eV. Comparing to Eq. (9), the dimensionless term f_j can be interpreted as an effective Born charge of the j th mode.

Substrate screening of excitons in MoS₂

As another illustration of the importance of substrate screening, we consider a monolayer of MoS₂ placed on top of an hBN substrate. We compare two different models for treating the substrate: In model 1, the substrate is represented by 100 layers of hBN building blocks. In model 2, the substrate is represented as a homogeneous bulk dielectric using the method of image charges as described in the theory section. The two models are sketched in Fig. 3(a). To account for the anisotropy of the hBN substrate, we use the geometric mean of the in- and out-of-plane dielectric constants $\epsilon(\omega) = \sqrt{\epsilon_z(\omega)\epsilon_{\parallel}(\omega)}$.⁴³ The bulk dielectric constants are obtained from RPA calculations employing the same parameter settings as used for the DBBs. We stress that we do not include phonons in these calculations, even though it would be straightforward to do so. The image plane of the bulk substrate is set at $-d$ relative to the center of the MoS₂ layer, where d denotes the interlayer spacing in bulk MoS₂.

In Fig. 3(b) we compare the dielectric function of the supported MoS₂ obtained with the

two substrate models, which shows good agreement for large $q > 0.1 \text{ \AA}^{-1}$. For $q > 0.005 \text{ \AA}^{-1}$ (see inset) the two models show good agreement except for a constant offset of about 5% most likely originating from the inclusion of hybridization in the bulk RPA calculation. For small $q < 0.005 \text{ \AA}^{-1}$ (see inset) model 1 reproduces the 2D limit $\epsilon(q = 0) = 1$ because the substrate is in fact a 2D film (albeit not atomically thin).¹¹ In contrast, with a bulk substrate the dielectric function converges to $(1 + \epsilon_{\text{hBN,bulk}})/2$ for $q \rightarrow 0$.

In Fig. 3(c) we compare the binding energies of the lowest bright exciton in the MoS₂ layer obtained with the two different substrate models. The exciton energies were calculated from the Mott-Wannier model as described in Latini et al.⁴⁴. Again, the two models are generally in good agreement. The small difference between the binding energies calculated with model 1 and model 2 originates from the 5% difference in dielectric functions and is not essential. The inclusion of a substrate predicts lower binding energies compared to free standing MoS₂, also in agreement with literature.⁴⁵ Increasing the number of hBN layers in the thin film substrate (model 1), the exciton binding energies converge towards a value very close to that obtained with the bulk substrate (model 2), see Fig. 3(d).

Hyperbolic plasmons in doped phosphorene

As a final example of the new implementation, we calculate the loss function of a single layer black phosphorus, see Fig. 4. It is well-known that the in-plane structural anisotropy of phosphorene is significantly reflected in the electronic and optical properties,^{46,47} meaning that the employed effective mass would be anisotropic as well (see Sec. S4 for details). The calculations employed a DBB with the effect of the free carriers described by the 2DEG response function with a doping concentration corresponding to $E_F = 0.05 \text{ eV}$, temperature of 300 K, and effective masses $m_y^* = 0.17m_0$ and $m_x^* = 1.12m_0$ (Sec. S3). The anisotropy is clearly seen in Fig. 4(a) where the different effective masses lead to different plasmon dispersion relations in the x and y directions, respectively. The white dashed lines indicate the limits of the Landau damping regions where the plasmons decay into electron-hole pairs.

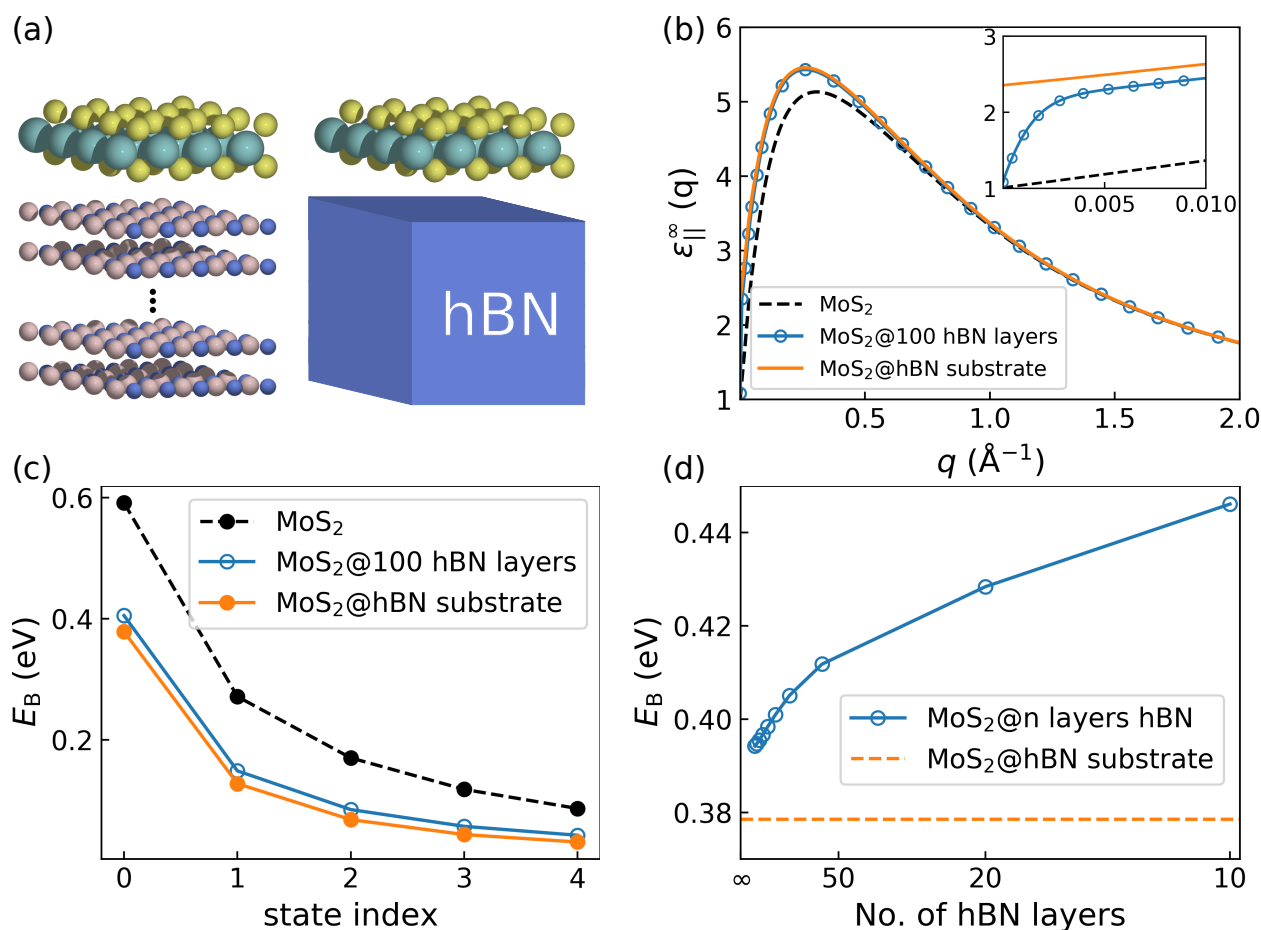


Figure 3: Effect of substrate screening on excitons in MoS₂. (a) We consider two different models for the substrate, namely n layers of hBN dielectric building blocks (model 1) and a homogeneous bulk dielectric (model 2). (b) Comparison of the dielectric function of the supported MoS₂ layer obtained with the two different substrate models. The dielectric function of freestanding MoS₂ is shown for comparison. The inset shows the screening for small values of q . (c) Binding energies of the lowest five s excitons in MoS₂. (d) Exciton binding energies for the lowest exciton in MoS₂ as function of the number of hBN layers included in model 1.

The anisotropy of phosphorene leads to hyperbolic isofrequency contours^{48,49} as shown in Figure 4(b). The isofrequency contours are plotted at two frequencies that lie inside and outside the hyperbolic frequency regime of $0.15 \text{ eV} < \hbar\omega < 0.35 \text{ eV}$, respectively. In these plots the size of the markers indicate the normalized plasmon propagation lengths (Sec. S5) showing that larger losses appear for the high momentum modes as they approach the Landau damped regions. Crucially, the inclusion of spatial non-locality limits the extend of the asymptotes, which would otherwise extend infinitely, and renormalizes the plasmonic density of states. An equivalent effect is observed in bulk metamaterials.⁵⁰

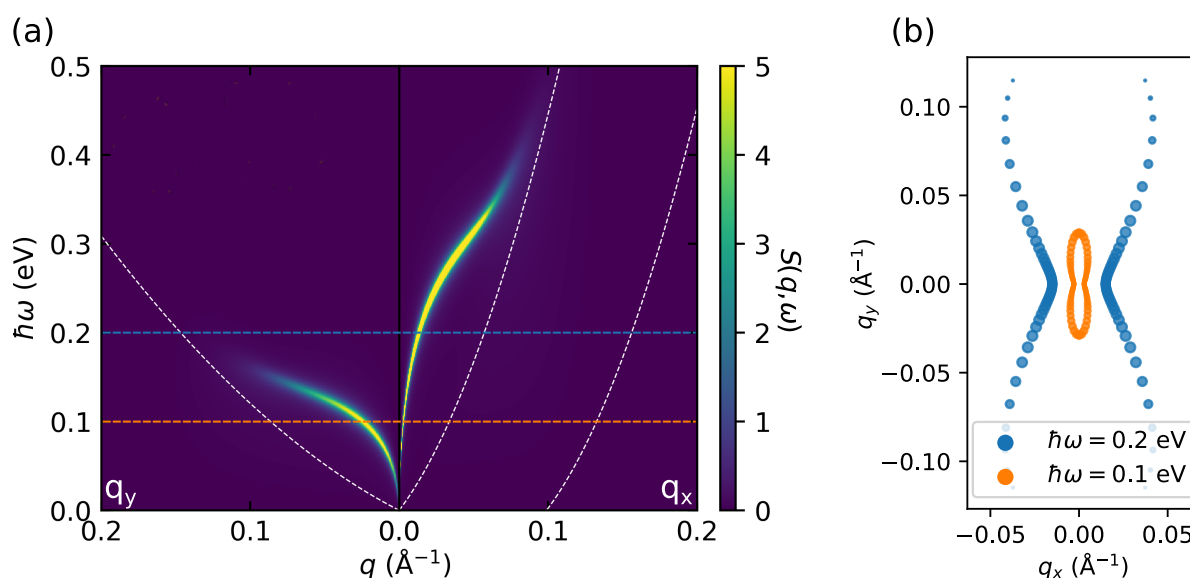


Figure 4: (a) Loss function of n-doped monolayer black phosphorus. The in-plane structural anisotropy is reflected by the different plasmon dispersion curves in the x and y directions. Dashed white lines indicate the Landau damped regions. (b) Isofrequency contours evaluated for $\hbar\omega = 0.1\text{eV}$ and $\hbar\omega = 0.2\text{eV}$ corresponding to the normal and hyperbolic frequency regimes, respectively.

Conclusions

In summary, we have introduced an extension of the quantum electrostatic heterostructure (QEH) model for calculating dielectric properties of 2D van der Waals heterostructures. The QEH model combines first-principles derived properties (electronic susceptibilities, phonons,

Born charges, effective masses) of the individual 2D layers with an efficient classical scheme to couple the layers via the Coulomb interaction, thereby avoiding the technical issues related to the full quantum mechanical description of lattice mismatched interfaces. The new developments allow for inclusion of screening from (polar) phonons, homogeneous bulk substrates/capping layers, and free carriers in the conduction or valence bands of doped semiconducting layers. The importance of including these screening sources for realistic modeling of plasmons, polar phonons and excitons was illustrated by several examples. The extensions significantly expand the applicability of the QEH model towards more experimentally relevant systems.

The basic structure of the QEH model remains unchanged and the new developments only affect the construction of the dielectric building blocks of the individual layers. The new QEH model is available as a standalone package written entirely in Python and comes with an improved user interface and a library of dielectric building blocks for the most common 2D materials. The QEH code and library is available at <https://pypi.org/project/qeh>.

Methods

Supporting information

Contents of supporting information:

- Sec. S1: Including lattice polarizability in the QEH formalism
- Sec. S2: Analytical dielectric building block for doped graphene
- Sec. S3: Inclusion of doped semiconductors in the QEH formalism
- Sec. S4: Density response function of anisotropic 2D semi-conductors
- Sec. S5: Plasmon propagation lengths in the QEH formalism

- Sec. S6: Inclusion of substrates in the QEH formalism
- Sec. S7: Technical details for Ab-Initio calculations

Acknowledgement

This study was partially supported by the Coordenação de Aperfeiçoamento de Pessoal de Nível Superior - Brasil (CAPES) - Finance Code 001. K.S.T. acknowledges funding from the European Research Council (ERC) under the European Union's Horizon 2020 research and innovation program (Grant Agreement No. 773122, LIMA). The Center for Nanostructured Graphene is sponsored by the Danish National Research Foundation (Project No. DNRF103).

References

- (1) Withers, F.; Del Pozo-Zamudio, O.; Mishchenko, A.; Rooney, A. P.; Gholinia, A.; Watanabe, K.; Taniguchi, T.; Haigh, S. J.; Geim, A. K.; Tartakovsky, A. I. et al. Light-emitting diodes by band-structure engineering in van der Waals heterostructures. *Nature Materials* **2015**, *14*, 301–306.
- (2) Massicotte, M.; Schmidt, P.; Vialla, F.; Schädler, K. G.; Reserbat-Plantey, A.; Watanabe, K.; Taniguchi, T.; Tielrooij, K. J.; Koppens, F. H. L. Picosecond photoresponse in van der Waals heterostructures. *Nature Nanotechnology* **2016**, *11*, 42–46.
- (3) Furchi, M. M.; Pospischil, A.; Libisch, F.; Burgdörfer, J.; Mueller, T. Photovoltaic Effect in an Electrically Tunable van der Waals Heterojunction. *Nano Letters* **2014**, *14*, 4785–4791.
- (4) Britnell, L.; Gorbachev, R. V.; Jalil, R.; Belle, B. D.; Schedin, F.; Mishchenko, A.; Georgiou, T.; Katsnelson, M. I.; Eaves, L.; Morozov, S. V. et al. Field-effect tunneling

- transistor based on vertical graphene heterostructures. *Science (New York, N.Y.)* **2012**, *335*, 947–50.
- (5) Georgiou, T.; Jalil, R.; Belle, B. D.; Britnell, L.; Gorbachev, R. V.; Morozov, S. V.; Kim, Y.-J.; Gholinia, A.; Haigh, S. J.; Makarovskiy, O. et al. Vertical field-effect transistor based on graphene-WS₂ heterostructures for flexible and transparent electronics. *Nature Nanotechnology* **2013**, *8*, 100–103.
- (6) Schmidt, P.; Vialla, F.; Latini, S.; Massicotte, M.; Tielrooij, K.-J.; Mastel, S.; Navickaite, G.; Danovich, M.; Ruiz-Tijerina, D. A.; Yelgel, C. et al. Nano-imaging of intersubband transitions in van der Waals quantum wells. *Nature Nanotechnology* **2018**, *13*, 1035–1041.
- (7) Bistritzer, R.; MacDonald, A. H. Moire bands in twisted double-layer graphene. *Proceedings of the National Academy of Sciences of the United States of America* **2011**, *108*, 12233–7.
- (8) Yankowitz, M.; Chen, S.; Polshyn, H.; Zhang, Y.; Watanabe, K.; Taniguchi, T.; Graf, D.; Young, A. F.; Dean, C. R. Tuning superconductivity in twisted bilayer graphene. *Science (New York, N.Y.)* **2019**, *363*, 1059–1064.
- (9) Cui, X.; Lee, G.-H.; Kim, Y. D.; Arefe, G.; Huang, P. Y.; Lee, C.-H.; Chenet, D. A.; Zhang, X.; Wang, L.; Ye, F. et al. Multi-terminal transport measurements of MoS₂ using a van der Waals heterostructure device platform. *Nature Nanotechnology* **2015**, *10*, 534–540.
- (10) Onida, G.; Reining, L.; Rubio, A. Electronic excitations: density-functional versus many-body Green's-function approaches. *Reviews of modern physics* **2002**, *74*, 601.
- (11) Thygesen, K. S. Calculating excitons, plasmons, and quasiparticles in 2D materials and van der Waals heterostructures. *2D Materials* **2017**, *4*, 022004.

- (12) Qiu, D. Y.; da Jornada, F. H.; Louie, S. G. Environmental screening effects in 2D materials: renormalization of the bandgap, electronic structure, and optical spectra of few-layer black phosphorus. *Nano letters* **2017**, *17*, 4706–4712.
- (13) Raja, A.; Chaves, A.; Yu, J.; Arefe, G.; Hill, H. M.; Rigosi, A. F.; Berkelbach, T. C.; Nagler, P.; Schüller, C.; Korn, T. et al. Coulomb engineering of the bandgap and excitons in two-dimensional materials. *Nature Communications* **2017**, *8*, 15251.
- (14) Cudazzo, P.; Tokatly, I. V.; Rubio, A. Dielectric screening in two-dimensional insulators: Implications for excitonic and impurity states in graphane. *Phys. Rev. B* **2011**, *84*, 085406.
- (15) Keldysh, L. Coulomb interaction in thin semiconductor and semimetal films. *Journal of Experimental and Theoretical Physics Letters* **1979**, *29*, 658.
- (16) Tran, K.; Moody, G.; Wu, F.; Lu, X.; Choi, J.; Kim, K.; Rai, A.; Sanchez, D. A.; Quan, J.; Singh, A. et al. Evidence for moiré excitons in van der Waals heterostructures. *Nature* **2019**, *567*, 71–75.
- (17) Seyler, K. L.; Rivera, P.; Yu, H.; Wilson, N. P.; Ray, E. L.; Mandrus, D. G.; Yan, J.; Yao, W.; Xu, X. Signatures of moiré-trapped valley excitons in MoSe₂/WSe₂ heterobilayers. *Nature* **2019**, *567*, 66.
- (18) Andersen, K.; Latini, S.; Thygesen, K. S. Dielectric genome of van der Waals heterostructures. *Nano Letters* **2015**, *15*, 4616–4621.
- (19) Xuan, F.; Chen, Y.; Quek, S. Y. Quasiparticle Levels at Large Interface Systems from Many-Body Perturbation Theory: The XAF-GW Method. *Journal of Chemical Theory and Computation* **2019**, *15*, 3824–3835.
- (20) Matthes, L.; Pulci, O.; Bechstedt, F. Influence of out-of-plane response on optical

- properties of two-dimensional materials: First principles approach. *Phys. Rev. B* **2016**, *94*, 205408.
- (21) Laturia, A.; Van de Put, M. L.; Vandenberghe, W. G. Dielectric properties of hexagonal boron nitride and transition metal dichalcogenides: from monolayer to bulk. *npj 2D Materials and Applications* **2018**, *2*, 6.
- (22) Nerl, H. C.; Winther, K. T.; Hage, F. S.; Thygesen, K. S.; Houben, L.; Backes, C.; Coleman, J. N.; Ramasse, Q. M.; Nicolosi, V. Probing the local nature of excitons and plasmons in few-layer MoS₂. *npj 2D Materials and Applications* **2017**, *1*, 2.
- (23) Resta, R. Macroscopic polarization in crystalline dielectrics: the geometric phase approach. *Reviews of modern physics* **1994**, *66*, 899.
- (24) King-Smith, R.; Vanderbilt, D. Theory of polarization of crystalline solids. *Physical Review B* **1993**, *47*, 1651.
- (25) Enkovaara, J.; Rostgaard, C.; Mortensen, J. J.; Chen, J.; Dułak, M.; Ferrighi, L.; Gavnholt, J.; Glinsvad, C.; Haikola, V.; Hansen, H. A. et al. Electronic structure calculations with GPAW: a real-space implementation of the projector augmented-wave method. *Journal of Physics: Condensed Matter* **2010**, *22*, 253202.
- (26) Hastrup, S.; Strange, M.; Pandey, M.; Deilmann, T.; Schmidt, P. S.; Hinsche, N. F.; Gjerding, M. N.; Torelli, D.; Larsen, P. M.; Riis-Jensen, A. C. et al. The Computational 2D Materials Database: high-throughput modeling and discovery of atomically thin crystals. *2D Materials* **2018**, *5*, 042002.
- (27) The dielectric building blocks and QEH software can be downloaded at <https://qeh.readthedocs.io/>.
- (28) Griffiths, D. J. *Introduction to electrodynamics*; Prentice Hall, 1999; p 576.

- (29) Novoselov, K. S.; Geim, A. K.; Guinea, F.; Peres, N. M. R.; Castro Neto, A. H. The electronic properties of graphene. *Reviews of Modern Physics* **2009**, *81*, 109–162.
- (30) Andersen, K.; Jacobsen, K. W.; Thygesen, K. S. Spatially resolved quantum plasmon modes in metallic nano-films from first-principles. *Physical Review B* **2012**, *86*, 245129.
- (31) Sohler, T.; Gibertini, M.; Calandra, M.; Mauri, F.; Marzari, N. Breakdown of optical phonons' splitting in two-dimensional materials. *Nano letters* **2017**, *17*, 3758–3763.
- (32) Tornatzky, H.; Gillen, R.; Uchiyama, H.; Maultzsch, J. Phonon dispersion in MoS₂. *Physical Review B* **2019**, *99*, 144309.
- (33) Koch, R. J.; Seyller, T.; Schaefer, J. A. Strong phonon-plasmon coupled modes in the graphene/silicon carbide heterosystem. *Physical Review B* **2010**, *82*, 201413.
- (34) Brar, V. W.; Jang, M. S.; Sherrott, M.; Lopez, J. J.; Atwater, H. A. Highly Confined Tunable Mid-Infrared Plasmonics in Graphene Nanoresonators. *Nano Letters* **2013**, *13*, 2541–2547.
- (35) Brar, V. W.; Jang, M. S.; Sherrott, M.; Kim, S.; Lopez, J. J.; Kim, L. B.; Choi, M.; Atwater, H. Hybrid Surface-Phonon-Plasmon Polariton Modes in Graphene/Monolayer h-BN Heterostructures. *Nano Letters* **2014**, *14*, 3876–3880.
- (36) Yan, H.; Low, T.; Zhu, W.; Wu, Y.; Freitag, M.; Li, X.; Guinea, F.; Avouris, P.; Xia, F. Damping pathways of mid-infrared plasmons in graphene nanostructures. *Nature Photonics* **2013**, *7*, 394–399.
- (37) Woessner, A.; Lundberg, M. B.; Gao, Y.; Principi, A.; Alonso-González, P.; Carrega, M.; Watanabe, K.; Taniguchi, T.; Vignale, G.; Polini, M. et al. Highly confined low-loss plasmons in graphene-boron nitride heterostructures. *Nature Materials* **2015**, *14*, 421–425.

- (38) Hajian, H.; Ghobadi, A.; Dereshgi, S. A.; Butun, B.; Ozbay, E. Hybrid plasmon–phonon polariton bands in graphene–hexagonal boron nitride metamaterials. *JOSA B* **2017**, *34*, D29–D35.
- (39) Laturia, A.; Vandenberghe, W. G. Dielectric properties of mono- and bilayers determined from first principles. 2017 International Conference on Simulation of Semiconductor Processes and Devices (SISPAD). 2017; pp 337–340.
- (40) Ashcroft, N. W.; Mermin, N. D. *Solid state physics*; Holt, Rinehart and Winston, 1976; p 826.
- (41) Luxmoore, I. J.; Gan, C. H.; Liu, P. Q.; Valmorra, F.; Li, P.; Faist, J.; Nash, G. R. Strong Coupling in the Far-Infrared between Graphene Plasmons and the Surface Optical Phonons of Silicon Dioxide. *ACS Photonics* **2014**, *1*, 1151–1155.
- (42) Gonçalves, P. A. D.; Peres, N. M. R. *An introduction to graphene plasmonics*; WORLD SCIENTIFIC, 2016.
- (43) Mele, E. J. Screening of a point charge by an anisotropic medium: Anamorphoses in the method of images. *American Journal of Physics* **2001**, *69*, 557–562.
- (44) Latini, S.; Olsen, T.; Thygesen, K. S. Excitons in van der Waals heterostructures: The important role of dielectric screening. *Physical Review B* **2015**, *92*, 245123.
- (45) Ugeda, M. M.; Bradley, A. J.; Shi, S.-F.; da Jornada, F. H.; Zhang, Y.; Qiu, D. Y.; Ruan, W.; Mo, S.-K.; Hussain, Z.; Shen, Z.-X. et al. Giant bandgap renormalization and excitonic effects in a monolayer transition metal dichalcogenide semiconductor. *Nature Materials* **2014**, *13*, 1091–1095.
- (46) Liu, H.; Neal, A. T.; Zhu, Z.; Luo, Z.; Xu, X.; Tománek, D.; Ye, P. D. Phosphorene: An Unexplored 2D Semiconductor with a High Hole Mobility. *ACS Nano* **2014**, *8*, 4033–4041.

- (47) Xia, F.; Wang, H.; Jia, Y. Rediscovering black phosphorus as an anisotropic layered material for optoelectronics and electronics. *Nature Communications* **2014**, *5*, 4458.
- (48) Nemilentsau, A.; Low, T.; Hanson, G. Anisotropic 2D Materials for Tunable Hyperbolic Plasmonics. *Phys. Rev. Lett.* **2016**, *116*, 066804.
- (49) Gomez-Diaz, J. S.; Tymchenko, M.; Alù, A. Hyperbolic Plasmons and Topological Transitions Over Uniaxial Metasurfaces. *Phys. Rev. Lett.* **2015**, *114*, 233901.
- (50) Yan, W.; Wubs, M.; Mortensen, N. A. Hyperbolic metamaterials: Nonlocal response regularizes broadband supersingularity. *Phys. Rev. B* **2012**, *86*, 205429.

Quantum Electrostatic Heterostructure




Figure 5: TOC Graphic.